Earth and Planetary Science Letters 395 (2014) 267–280

Contents lists available at ScienceDirect

Earth and Planetary Science Letters

www.elsevier.com/locate/epsl

Differentiation of Vesta: Implications for a shallow magma ocean

Wladimir Neumann [a,*], Doris Breuer [a], Tilman Spohn [a,b]

[a] Institute of Planetary Research, German Aerospace Center (DLR), Rutherfordstraße 2, 12489 Berlin, Germany
[b] Institute of Planetology, Westfälische Wilhelm-University Münster, Wilhelm-Klemm-Str. 10, 48149 Münster, Germany

ARTICLE INFO

Article history:
Received 29 May 2013
Received in revised form 25 February 2014
Accepted 15 March 2014
Available online xxxx
Editor: C. Sotin

Keywords:
asteroids, composition, dynamics
interiors
meteorites
planetary dynamics
planetary formation
planetesimals

ABSTRACT

The Dawn mission confirms earlier predictions that the asteroid 4 Vesta is differentiated with an iron-rich core, a silicate mantle and a basaltic crust, and supports the conjecture of Vesta being the parent body of the HED meteorites. To better understand its early evolution, we perform numerical calculations of the thermo-chemical evolution adopting new data obtained by the Dawn mission such as mass, bulk density and size of the asteroid.

We have expanded the thermo-chemical evolution model of Neumann et al. (2012) that includes accretion, compaction, melting and the associated changes of the material properties and the partitioning of incompatible elements such as the radioactive heat sources, advective heat transport, and differentiation by porous flow, to further consider convection and the associated effective cooling in a potential magma ocean. Depending on the melt fraction, the heat transport by melt segregation is modelled either by assuming melt flow in a porous medium or by simulating vigorous convection and heat flux of a magma ocean with a high effective thermal conductivity.

Our results show that partitioning of ^{26}Al and its transport with the silicate melt is crucial for the formation of a global and deep magma ocean. Due to the enrichment of ^{26}Al in the liquid phase and its accumulation in the sub-surface (for formation times $t_0 < 1.5$ Ma), a thin shallow magma ocean with a thickness of 1 to a few tens of km forms – its thickness depends on the viscosity of silicate melt. The lifetime of the shallow magma ocean is O(10^4)–O(10^6) years and convection in this layer is accompanied by the extrusion of ^{26}Al at the surface, resulting in the formation of a basaltic crust. The interior differentiates from the outside inwards with a mantle that is depleted in ^{26}Al and core formation is completed within ~0.3 Ma. The lower mantle experiences a maximal melt fraction of 45% suggesting a harzburgitic to dunitic composition. Our results support the formation of non-cumulate eucrites by the extrusion of early partial melt while cumulate eucrites and diogenites may form from the crystallising shallow magma ocean. Silicate melt is present in the mantle for up to 150 Ma, and convection in a crystallising core proceeds for approximately 100 Ma, supporting the idea of an early magnetic field to explain the remnant magnetisation observed in some HED meteorites.

© 2014 Elsevier B.V. All rights reserved.

1. Introduction

The large asteroid 4 Vesta, located in the inner belt at a mean heliocentric distance of 2.36 AU, is the second-most-massive body in the asteroid belt. Ground-based observations indicate a dry, basaltic surface composition, suggesting that melt segregation and core–mantle differentiation must have taken place and that the body has been resurfaced by basaltic lava flows (e.g. Zellner et al., 1997). The Dawn mission recently orbiting Vesta confirms this observation and the notion that this asteroid is the parent body of the HED (howardite, eucrite and diogenite) meteorites (De Sanctis et al., 2012; Russell et al., 2013). HEDs consist mainly of non-cumulate eucrites (pigeonite–plagioclase basalts) and orthopyroxene-rich diogenites. Howardites are impact breccias, composed predominantly of eucrite and diogenite clasts. The igneous lithology is completed with more rare rock types that include cumulate eucrites and olivine-bearing diogenites. This lithology has been used to constrain the interior structure. Vesta is believed to have a layered structure consisting of at least a metallic core, a rocky olivine-rich mantle and a crust consisting mainly of an upper basaltic (eucritic) and a lower orthopyroxene-rich layer (e.g. Delaney, 1995; Ruzicka et al., 1997; Righter and Drake, 1997; Mandler and Elkins-Tanton, 2013). The details in the interior structure vary between the models and depend among others on the assumption of the bulk composition of Vesta. A eucritic upper crust

* Corresponding author. Tel.: +49 3067055395; fax: +49 3067055303.
E-mail addresses: Wladimir.Neumann@dlr.de (W. Neumann), Doris.Breuer@dlr.de (D. Breuer), Tilman.Spohn@dlr.de (T. Spohn).

http://dx.doi.org/10.1016/j.epsl.2014.03.033
0012-821X/© 2014 Elsevier B.V. All rights reserved.

and orthopyroxene-rich lower crust have been also identified by Dawn, in particular, in the Rheasilvia basin (De Sanctis et al., 2012; Prettyman et al., 2012). The huge basin allows the identification of material that was formed down to a depth of 30–45 km and has been excavated or exposed by an impact (Jutzi and Asphaug, 2011; Ivanov and Melosh, 2013). Interestingly, olivine-rich and, thus, mantle material has not been found in a significant amount, i.e. not above the detection limit of <25%, suggesting a crustal thickness of at least 30–45 km (McSween et al., 2013). This finding may also explain the lack of olivine-rich samples in the HED collection. It should be noted, though, that several olivine-rich terrains were actually detected by Dawn in the northern hemisphere (De Sanctis et al., 2013; Ruesch et al., 2013).

Two possible differentiation scenarios have been associated with the formation of the basaltic achondrites (i.e., eucrites and diogenites). The first scenario suggests that eucrites and diogenites originated from the partial melting of the silicates (e.g. Stolper, 1975, 1977; Jones, 1984; Jones et al., 1996) with the extraction of basaltic (euritic) magma leaving behind a harzburgite, orthopyroxenite or dunite residual depending on the degree of partial melting. The other scenario favoured by geochemical arguments suggests achondrites being cumulates formed by magma fractionation. In the latter scenario the diogenites could have crystallised either in a magma ocean (Ikeda and Takeda, 1985; Righter and Drake, 1997; Ruzicka et al., 1997; Takeda, 1997; Warren, 1997; Drake, 2001; Greenwood et al., 2005; Schiller et al., 2011) or in multiple, smaller magma chambers (Shearer et al., 1997; Barrat et al., 2008; Beck and McSween, 2010; Mandler and Elkins-Tanton, 2013). Eucrites are then products from the magmas that had earlier crystallised diogenites.

Eucrites exhibit siderophile depletions that indicate the formation of an iron-rich core prior to their crystallisation and within ~1 to 4 Ma of the beginning of the solar system (Palme and Rammensee, 1981; Righter and Drake, 1997; Kleine et al., 2009). Assuming core densities between 7000 and 8000 $\mathrm{kg\,m^{-3}}$, the core radius of Vesta is estimated to lie between 105 and 114 km (Raymond et al., 2012; Russell et al., 2012), approximately half of the asteroid's radius. Some HEDs (e.g. Millbillillie and Allan Hills A81001), furthermore, show a remnant magnetisation suggesting a formerly active dynamo in a liquid metallic core (Fu et al., 2012a, 2012b).

To understand Vesta's thermal and geological evolution, several numerical and experimental studies (e.g. Righter and Drake, 1997; Ghosh and McSween, 1998; Drake, 2001; Gupta and Sahijpal, 2010) have been performed. Questions these studies want to answer are related to the timing of accretion and core formation and the history of volcanism, especially the formation of the basaltic crust. Related to the last issue is, in particular, the question about the origin of the HED meteorites that either originated from the partial melting of the silicates or are residual melts of a crystallising and formerly convecting whole-mantle magma ocean. It should be noted, though, that in most models the formation of core and crust has not been modelled self-consistently; rather some specific scenario has been assumed and its consequences for the thermal evolution on Vesta have been studied.

Righter and Drake (1997) considered core formation and crystallisation of a cooling magma ocean using a numerical physicochemical model. They suggested that after cooling to a crystal fraction of 80%, residual melt percolated from the former extensive magma ocean to form eucrites at the surface and diogenites in shallow layers by further crystallisation. In their model complete crystallisation occurred within 20 Ma after the formation of Vesta.

Ghosh and McSween (1998) investigated the differentiation of Vesta by assuming instantaneous core formation in the temperature interval of 1213–1223 K (assumed solidus and liquidus temperature of Fe–FeS) and that HED meteorites are the product of 25% partial melting. To obtain such a scenario, they concluded that Vesta must have accreted at 2.85 Ma, differentiated at 4.58 Ma and formed a basaltic crust at 6.58 Ma relative to the formation of the CAIs. Furthermore, they suggested that the mantle remained hot for 100 Ma after its formation and that some near-surface layers may have remained undifferentiated.

The latter models suggesting a global magma ocean neglect efficient cooling due to convection in the magma ocean and partitioning of ^{26}Al into the silicate melt and of its migration towards the surface. So far, there have not been many attempts to model magma ocean convection in planetesimals. A first model to study the influence of a convecting magma ocean that formed due to heating by ^{26}Al in planetesimals with radii of less than 100 km was presented by Hevey and Sanders (2006). Convection and the associated heat transport have been simulated by increasing the thermal conductivity by three orders of magnitude upon reaching a melt fraction of 50% – at this rheologically critical melt fraction (RCMF) a strong decrease in the viscosity is expected, resulting in vigorous convection and efficient heat transport (Marsh, 1988). As an important consequence, it has been shown that the excess radiogenic heating does not raise the temperature of the convecting interior. Thus, not the degree of the partial melting in the magma ocean, but rather the extent of the molten zone increases.

Gupta and Sahijpal (2010) adopted this approach in their simulations for Vesta by varying the thermal diffusivity by three orders of magnitude between the melt fractions of 50% and 100% (thereby, the thermal conductivity was increased). They investigated two evolution paths, namely the formation of basaltic achondrites in Vesta via partial melting of silicates or as residual melts after crystallisation of a convecting magma ocean. They concluded that, depending on the formation time, melt extraction is possible between 0.15 and 6 Ma after the CAIs and that differentiation proceeds rapidly within $O(10^4)$ a. For the scenarios where accretion was completed within 2 Ma after the CAIs, a magma ocean formed, which did not crystallise completely for at least 6–10 Ma. We will later show that for magma oceans comprising a large part of the mantle, the convective heat flux is underestimated in the studies Hevey and Sanders (2006) and Gupta and Sahijpal (2010) in comparison to that of the soft turbulence regime that is valid when the viscosity is small and convection is extremely turbulent, as in the case of magma oceans (Solomatov, 2007). In fact, as we point out further below, the effective thermal conductivity of the magma ocean is underestimated by up to three orders of magnitude.

The importance of equilibrium partitioning of ^{26}Al into the silicate melt and of its migration toward the surface has been shown by Moskovitz and Gaidos (2011) for planetesimals smaller than Vesta. They concluded that migration of ^{26}Al-enriched melt towards the surface inhibits a further increase of internal temperatures and partial melting. In their model, only subsequent heating by ^{60}Fe generates melt fractions of over 50% completing the differentiation of the bodies of interest. Although Vesta was not considered in their study, the partitioning of ^{26}Al, its extrusion to the surface and the associated depletion of the interior would have a strong impact on its thermal evolution.

As a general conclusion from the previous thermal models, one can state that Vesta should have finished its accretion by ≈3 Ma after the CAIs due to the decrease of the radiogenic heating by ^{26}Al and ^{60}Fe with time. Whether the basaltic crust, i.e. eucrites and diogenites, did form after the core–mantle separation due to the crystallisation of a global magma ocean (residual melt origin) or prior to the core–mantle separation due to the extrusion of the first partial melts (partial melting origin) remains an open issue, although geochemical models suggest that core formation precedes crust formation (e.g. Kleine et al., 2009). Which scenario is more likely also depends on the competition between heating by

short-lived isotopes and the depletion of these heat sources due to their partitioning into the melt and the migration velocity of this melt by porous flow. Only if the extrusion of melt containing ^{26}Al was comparatively slow, an asteroid-scale magma ocean may have formed, otherwise HEDs formed by the extrusion of early partial melts. In case of a magma ocean, its convective cooling and the associated thermal convection in the core could result in a core dynamo lasting for several 10 Ma if Vesta formed before ≈1.5 Ma after the CAIs (Elkins-Tanton et al., 2011) although Sterenborg and Crowley (2013) argue that only parent bodies larger than 500 km can produce a sufficiently strong magnetic field longer than 10 Ma by thermal convection.

In the present study, we investigate the thermal evolution of Vesta by means of a comprehensive model that includes melting, associated changes of the material properties, differentiation via porous flow and the corresponding advective heat transport below the RCMF of 50% (Marsh, 1988), as well as convection and the associated effective cooling in a magma ocean and liquid core for melt fractions above the RCMF applying the soft-turbulence approach (Solomatov, 2007). Numerical calculations of the thermochemical evolution of Vesta are performed adopting the new data obtained by the Dawn mission (e.g. the mass, the bulk density and the dimensions, see Russell et al., 2012). In particular, we investigate the occurrence and the time scale of core–mantle differentiation, the differences between the models that consider partitioning of ^{26}Al and those that neglect partitioning of ^{26}Al, as well as the influence of the convecting magma ocean on the thermal evolution of Vesta. We conclude that due to the extrusion of ^{26}Al towards the surface a thin sub-surface magma ocean forms prior to the completion of the core–mantle differentiation and that the depleted mantle remains below the RCMF.

2. Model description

The evolution of an asteroid begins with its accretion from the protoplanetary dust as a porous aggregate. Heating by radioactive decay combined with self-gravity leads to substantial compaction at sub-solidus temperatures. Provided strong heating, the metal phase and, subsequently, the silicate phase starts to melt upon reaching the respective solidus temperatures. The radioactive isotope ^{26}Al partitions among other incompatible elements into the silicate melt. If melting is wide-spread enough, the asteroid can differentiate (at least partially) via porous flow into a metallic core and a silicate mantle. Differentiation is initiated by the iron melt sinking downward and silicate melt percolating towards the surface. The mantle and core regions, in which the partial melt increases above 50%, start convecting. Furthermore, convection starts only when the heat flow at the upper interface becomes superadiabatic – this is, in particular, a limiting factor for convection in the core. The asteroid cools first due to convection and after the melt fractions drop below 50% by conduction as well as melt heat transport to the sub-solidus temperatures. After cooling below the solidus, no further structural changes (differentiation) of the interior can be expected except by external influence such as impacts.

To model the above evolution path for Vesta, we have adopted the thermal evolution model from Neumann et al. (2012) which considers accretion, compaction, melting and differentiation by porous flow of ordinary chondritic planetesimals. For a detailed description of the model we refer to Neumann et al. (2012) and Neumann et al. (2013). Next, we give a brief summary of the important model features and describe, in particular, the additional processes implemented for the current study as well as the parameters that are specific for Vesta.

The rate of change of internal energy, including the consumption and release of latent heat due to melting and solidification is computed from the conductive heat flow, the volumetric heat production rate by radioactive decay, and the advective heat transport by melt percolation:

$$\rho c_p (1 + x_{\mathrm{Fe}} Ste_{\mathrm{Fe}} + x_{\mathrm{Si}} Ste_{\mathrm{Si}}) \frac{\partial T}{\partial t} = \vec{\nabla}\left(k(\vec{x})\vec{\nabla}T\right) + Q(\vec{x}, t) + \vec{\nabla}T(\Delta v_{\mathrm{Fe}} + \Delta v_{\mathrm{Si}}), \quad (1)$$

where ρ is the density, c_p is the specific heat capacity, x_{Fe} and x_{Si} are the current mass fractions of metallic iron and silicates, respectively, Ste_{Fe} and Ste_{Si} are the Stefan numbers of metal and silicates, respectively, T is temperature, t is time, $\vec{x}$ is the space variable, k is the thermal conductivity, Q is the heat source density, and Δv_{Fe} and Δv_{Si} are the velocities of iron and silicate melts relative to the matrix, respectively.

Because we consider porosity loss during the thermal evolution, the initial radius R_p of the body changes to the compacted radius $\bar{R}_p(t) = R_p\left(\frac{1-\phi_0}{1-\bar{\phi}(t)}\right)^{1/3}$, where $\bar{\phi}(t)$ is the average porosity at time t, and ϕ_0 is the uniform initial porosity (see Neumann et al., 2012). The average porosity $\bar{\phi}(t)$ and the average density $\bar{\rho}(t)$ are computed using the equations $\bar{\phi}(t) = 1 - V_i/V_b$ and $\bar{\rho}(t) = M/V_b$ where V_i is the intrinsic volume (i.e., the volume of the solid material), V_b is the bulk volume (i.e., the volume of the solid material plus the volume of the pores, computed by integrating the porosities at the grid points of the discretisation over the body) and M is the mass of Vesta.

The thermal conductivity, density, heat source density, radius, and some other parameters change with time due to the loss of porosity and melting. The loss of the porosity ϕ is a consequence of compaction by hot-pressing under the influence of temperature and pressure:

$$\frac{\partial \log(1 - \phi(\vec{x}))}{\partial t} = A\sigma^{3/2} b^{-3} e^{-E/RT}, \quad (2)$$

where $A = 4.0 \cdot 10^{-5}$ bar$^{-3/2}$ cm^3 s^{-1} is a constant, σ is the effective stress acting on a unit volume in bar, $b = 10^{-4}$ cm is the initial grain size, $E = 272$ kJ mol^{-1} is the activation energy, and $R = 0.00831$ kJ mol^{-1} K^{-1} is the universal gas constant (see Schwenn and Goetze, 1978).

Iron or silicate melt is generated linearly between the solidus and the liquidus temperatures of metal or silicates. In these temperature intervals both components are present in both solid and liquid states. Consumption and release of the latent heat during the melting and solidification buffers temperature variations between the entirely solid and the entirely liquid state.

In terms of the flow in porous media theory, we relocate the intrinsically denser (than the bulk solid matrix) metal melt downwards, and the intrinsically lighter silicate melt towards the surface, according to Darcy's law. This approach is valid below the RCMF. In this case, the energy transport by the melts enters into the heat conservation equation via advection terms. Thereby, the associated grain growth due to Ostwald ripening is accounted for in the partially molten regions of the body resulting in faster percolation velocities with time.

Assuming equilibrium melting, the chemical partitioning of ^{26}Al is described by

$$c^{tot}_{\mathrm{Al}} = \chi_{\mathrm{Si}} c^{l}_{\mathrm{Al}} + (1 - \chi_{\mathrm{Si}}) c^{s}_{\mathrm{Al}}, \qquad c^{l}_{\mathrm{Al}} = \frac{c^{tot}_{\mathrm{Al}}}{P + \chi_{\mathrm{Si}}(1 - P)},$$
$$c^{s}_{\mathrm{Al}} = \frac{c^{tot}_{\mathrm{Al}} P}{P + \chi_{\mathrm{Si}}(1 - P)}, \quad (3)$$

with the total concentration of ^{26}Al c^{tot}_{Al}, the concentration in the solid and liquid phase c^{s}_{Al} and c^{l}_{Al}, the melt fraction of silicates (relative to the overall amount of silicates) χ_{Si}, and the partitioning coefficient P (Best, 2002).

Table 1
Composition, density and thermal conductivity.

Phase	Mineral	Mass fraction (%)	Volume fraction (%)	ρ_{solid} (kg m^{-3})	ρ_{liquid} (kg m^{-3})	k (W m^{-1} K^{-1})
Metal	–	**14**	**7.79**	**6471.12**	**5490.88**	**10.2**
	Fe	8	–	7874	6980.00	21.0
	Ni	1	–	8908	7810.00	21.0
	FeS	5	–	4830	3920.00	4.6
Silicates	–	**86**	**92.21**	**3357**	**2900**	**3.8**
	Olivine	49	–	3510.00	–	4.3
	orthopyroxene	23	–	3380.00	–	3.9
	clinopyroxene	6	–	3320.00	–	4.6
	Plagioclase	8	–	2630.00	–	1.9
Total	**L-chondrite**	**100**	**100**	**3600.05**	**3105.12**	**4.2**

This data is for the most part from Yomogida and Matsui (1983) for L-chondrites.

To calculate the initial composition of the primordial material we assume that Vesta formed from L-chondritic material. The minerals, their mass fractions and densities are taken from Yomogida and Matsui (1983) (see Table 1). The metal phase consists of free iron and nickel and of the troilite. The remaining minerals form the silicate phase. This composition is a reasonable choice considering Dawn's measurements of the density. First, a metal mass fraction of 0.14 in an L-chondritic composition results in a relative core radius of ≈0.43 if one assumes complete differentiation, which agrees with the core radius of Vesta suggested by Russell et al. (2012). Note that for an H-chondritic composition a larger core with a relative core radius of ≈0.49 would follow (cf. Neumann et al., 2012). Second, the average bulk density of 3456 ± 34 kg m^{-3} (Russell et al., 2012) lies slightly below a typical intrinsic density of an L-chondrite (see Yomogida and Matsui, 1983), which is approximately 3600 kg m^{-3} (cp. Table 1).

Heavy cratering of the surface suggests a porous upper mantle and crust. Russell et al. (2012) suggested a porosity of 5–6% in these layers, which means that the average porosity of the entire body is smaller. From $\rho_i = \rho_b(1-\phi)^{-1}$, where ρ_i is the average intrinsic density and ρ_b is the bulk density, the average porosity of Vesta ϕ can be calculated. For $\rho_b = 3490$ kg m^{-3}, which is the smallest upper bound, we obtain $\phi = 0.03$, and for $\rho_b = 3456$ kg m^{-3}, $\phi = 0.04$ follows. This would mean that the average porosity of the mantle and the crust of Vesta is larger than 4%. The bulk density ρ_{b0} of the primordial material during the accretion of Vesta is calculated by using a reasonable uniform initial porosity $\phi_0 = 0.4$ of the accreting material (see Henke et al., 2012; Neumann et al., 2012) and the equation $\rho_{b0} = (1-\phi_0)\rho_i$. For $\rho_i = 3600$ kg m^{-3} we obtain $\rho_{b0} = 2160$ kg m^{-3}.

Taking the volume of Vesta as $7.497 \cdot 10^7$ m^3 (Russell et al., 2012) and assuming a negligible average porosity (in our most realistic calculations Vesta compacted almost completely; this is a result of our model runs), a radius of 262 km is obtained. We take this as a reference value that corresponds to a completely compacted body. For an appropriate choice of the average present-day porosity the value of 262.7 ± 0.1 inferred by Russell et al. (2012) follows. Note, though, that a body with the axes of 572.6 by 557.2 by 446.4 km is considered here to be spherically symmetric. Our model combines the average (uniform) initial porosity of $\phi_0 = 0.4$ with the reference radius of $D = 262$ km to obtain the initial radius of $R_p = 310$ km.

For melt fractions above 50%, the settling velocity v_s of the molten iron globules or solid iron crystals in a silicate "mush" is computed via Stokes' law

$$v_s = \frac{2}{9}\frac{\rho_g - \rho_m}{\eta_{l,\mathrm{Si}}} g b^2, \tag{4}$$

where ρ_g is the density of a metal globule (liquid iron), ρ_m is the density of the silicate "mush" (liquid silicate), $\eta_{l,\mathrm{Si}}$ is the viscosity of the liquid silicates, g is the gravitational acceleration and b is the radius of a metal globule (here a constant value of 0.01 m is adopted, see e.g. Samuel, 2012 and Taylor, 1992 for the globule size). Strictly speaking, further dynamic regimes (Newton and intermediate regimes, see Samuel, 2012) should be considered besides the Stokes regime. Our estimates using parameters from Tables 1 and 2 indicate that the velocities obtained in the Stokes, Newton or intermediate regimes are very similar and much higher compared to the Darcy velocity obtained below the RCMF (the latter is orders of magnitude smaller). The metal separation is, thus, almost instantaneous for the situation of high melt fraction and we therefore consider only the Stokes regime.

Throughout the study the nebula temperature of $T_n = 290$ K (this value corresponds to the temperature in the Solar nebula at 2.36 AU, see Ghosh and McSween, 1998) is used as the initial temperature of the accreting material and also for the boundary condition. The radiation boundary condition is adopted with the emissivity $e = 0.8$ (Ghosh and McSween, 1998).

For a body which formed during the first few million years after the formation of the Solar system the short-lived isotopes ^{26}Al and ^{60}Fe are believed to be the most important heat sources. Whereas most researchers suggest the "canonical" ratio $[^{26}\mathrm{Al}/^{27}\mathrm{Al}]_0 = 5 \cdot 10^{-5}$ at the time of the formation of CAIs, there is still an uncertainty about the initial ratio $[^{60}\mathrm{Fe}/^{56}\mathrm{Fe}]_0$ (values between 10^{-8} and 10^{-6} have been inferred by numerous workers). For ^{26}Al we use the canonical ratio $[^{26}\mathrm{Al}/^{27}\mathrm{Al}]_0 = 5 \cdot 10^{-5}$ at the formation of the CAIs, and for ^{60}Fe the value $[^{60}\mathrm{Fe}/^{56}\mathrm{Fe}]_0 = 1.6 \cdot 10^{-6}$ reported by Cameron (1993). As this value is highly uncertain and recent experiments suggest that previous measurements are likely biased and predict too high values of $[^{60}\mathrm{Fe}/^{56}\mathrm{Fe}]_0$ (Ogliore et al., 2011; Telus et al., 2012), we further study the influence of the amount of ^{60}Fe on the results.

Apart from the initial ratios above, the heat production rate depends on the abundance of Al and Fe in the bulk material. The latter are computed from the exact composition and fractions of metal and silicates (see further below). The heat sources density term $Q(r,t)$ in the energy balance equation (1) arises from the radiogenic decay of ^{26}Al and ^{60}Fe. We write this term as

$$Q(r,t) = \rho\left(v_{\mathrm{Si}}\left[\frac{^{26}\mathrm{Al}}{^{27}\mathrm{Al}}\right]_0 \frac{E_{\mathrm{Al}}}{\tau_{\mathrm{Al}}} e^{-\frac{t+t_0}{\tau_{\mathrm{Al}}}} + \frac{x_{\mathrm{Fe}}}{x_{\mathrm{Fe},0}} f_{\mathrm{Fe}}\left[\frac{^{60}\mathrm{Fe}}{^{56}\mathrm{Fe}}\right]_0 \frac{E_{\mathrm{Fe}}}{\tau_{\mathrm{Fe}}} e^{-\frac{t+t_0}{\tau_{\mathrm{Fe}}}}\right), \tag{5}$$

where $v_{\mathrm{Si}} = f_{\mathrm{Al}} x_{\mathrm{Si}}/x_{\mathrm{Si},0}$ (prior to silicate melting, partitioning and melt segregation), $x_{\mathrm{Fe},0}$ and $x_{\mathrm{Si},0}$ are the initial mass fractions of metal and silicates, f_{Fe} and f_{Al} are the numbers of iron or aluminium atoms per 1 kg of the primordial material, respectively, E_i is the decay energy per atom, τ_i is the mean life, $[^*i/^*i]_0$ is the initial abundance of the isotope $^*i$, and t_0 is the delay time of accretion with respect to the formation time of the CAIs. The mass fraction ratios control the changes in the heat production due to

Table 2
Parameter values used for the models.

Quantity	Symbol	Unit	Value	Reference
Initial porosity	ϕ_0	–	0.4	1
Reference radius	D	km	262	2
Initial radius	R_p	km	310	2
Thermal expansivity of iron	α_{Fe}	K^{-1}	$7.70 \cdot 10^{-5}$	3
Thermal expansivity of silicates	α_{Si}	K^{-1}	$2.00 \cdot 10^{-5}$	4
Iron melt viscosity	$\eta_{l,\mathrm{Fe}}$	Pa s	10^{-2}	1
Silicate melt viscosity	$\eta_{l,\mathrm{Si}}$	Pa s	1	1
Metal solidus temperature	$T_{S,\mathrm{Fe}}$	K	1213	1
Metal liquidus temperature	$T_{L,\mathrm{Fe}}$	K	1700	1
Silicate solidus temperature	$T_{S,\mathrm{Si}}$	K	1425	1
Silicate liquidus temperature	$T_{L,\mathrm{Si}}$	K	1850	1
Radius of iron globules	b	m	0.01	2
Partitioning coefficient	P	–	0.02	1
Stefan-Boltzmann constant	σ_{SB}	$\mathrm{W\,m^{-2}\,K^{-4}}$	$5.67 \cdot 10^{-8}$	–
Emissivity	E	–	0.8	5
Avogadro number	N_A	mol^{-1}	$6.02 \cdot 10^{23}$	–
Nebula temperature	T_N	K	290	1
Decay energy per atom of ^{26}Al	$E_{^{26}\mathrm{Al}}$	J	$6.41 \cdot 10^{-13}$	1
Decay energy per atom of ^{60}Fe	$E_{^{60}\mathrm{Fe}}$	J	$4.87 \cdot 10^{-13}$	1
Initial abundance of ^{26}Al	$f_{^{26}\mathrm{Al}}$	kg^{-1}	$2.76 \cdot 10^{23}$	2
Initial abundance of ^{60}Fe	$f_{^{60}\mathrm{Fe}}$	kg^{-1}	$1.12 \cdot 10^{24}$	2
Mass fraction of bulk Al	m_{Al}	%	1.19	2
Mass fraction of bulk Fe	m_{Fe}	%	11.18	2
Initial ratio of ^{26}Al	$[^{26}\mathrm{Al}/^{27}\mathrm{Al}]_0$	–	$5 \cdot 10^{-5}$	1
Initial ratio of ^{60}Fe	$[^{60}\mathrm{Fe}/^{56}\mathrm{Fe}]_0$	–	$1.6 \cdot 10^{-6}$	1
Half-life of ^{26}Al	$\tau_{1/2}(^{26}\mathrm{Al})$	Ma	0.717	1
Half-life of ^{60}Fe	$\tau_{1/2}(^{60}\mathrm{Fe})$	Ma	2.61	6

References: 1 Neumann et al. (2012). 2 Model section. 3 Rivoldini et al. (2011). 4 Sohl and Spohn (1997). 5 Ghosh and McSween (1998). 6 Rugel et al. (2009).

the differentiation. The bulk Al mass fraction is calculated from that of Al_2O_3 in L-chondrites reported by Jarosevich (1990). The latter value of 0.0225 is multiplied with the ratio of the atomic mass of ^{27}Al (in $\mathrm{g\,mol}^{-1}$) times two to the sum of the atomic masses of ^{27}Al times two and ^{16}O times three, to obtain the value of 0.0119. This is slightly larger than the value of 0.0113 used by Ghosh and McSween (1998) for Vesta, because they assumed an H-chondritic composition and adopted the Al_2O_3 mass fraction of 0.0214 from Jarosevich (1990).

The mass fraction of the bulk iron is computed from the mass fraction of the free iron Fe and the mass fraction of FeS times the ratio of the atomic mass of Fe and the sum of the atomic masses of Fe and S. Thereupon, the (initial) abundances are computed using the formulas $f_{\mathrm{Al}} = 10^3 m_{\mathrm{Al}} N_A (ma_{^{26}\mathrm{Al}})^{-1}$ (before melting and partitioning) and $f_{\mathrm{Fe}} = 10^3 m_{\mathrm{Fe}} N_A (ma_{^{60}\mathrm{Fe}})^{-1}$, where m_{Al} and m_{Fe} are mass fraction of the elements, $ma_{^{26}\mathrm{Al}}$ and $ma_{^{60}\mathrm{Fe}}$ are the atomic masses of the heat generating isotopes, and N_A is the Avogadro number (for the resulting values see Table 2). The factor v_{Si} controls, on the one hand, the changes in the silicate mass fraction due to the migration of the silicate melt as compared to the initial mass fraction. On the other hand, this factor updates the changes in the concentration of ^{26}Al in a given discretisation shell, which arise from the mixing of migrated and present melt with different concentration of ^{26}Al and from the matrix compaction. Once melt segregation starts, ^{26}Al particles associated with the migrated silicate melt from a lower shell are added to those remaining in the upper shell after the compaction of the mixed metal–silicate-matrix. The number of ^{26}Al particles in the lower shell is updated to account for the ^{26}Al that left with the silicate melt and the particles added due to the matrix compaction. Similarly, as iron melt moves from an upper shell to a lower one and is being replaced by either a certain volume of the matrix or/and a certain volume of the silicate melt, the number of ^{26}Al particles is updated due to these volume changes. We have neglected the heating by ^{60}Fe which remains in the silicate phase after core formation; its contribution to the heating of the mantle is, however, negligible.

As in the previous studies, we do not consider the solid-state convection for melt fractions below 50%. In order to model the convection in a magma ocean, where more than 50% of the material is molten, we adopt the method presented in Solomatov (2007) (see also Kraichnan, 1962 and Siggia, 1994) to compute the convective heat flux in the soft turbulence regime (when the viscosity is small and convection is extremely turbulent, but the Rayleigh number is still below approximately 10^{19}). This approach has also been used for modelling of local magma ponds on Mars (Golabek et al., 2011). From the convective heat flux the effective thermal conductivity is calculated. The thermal conductivity in the magma ocean is substituted by the effective thermal conductivity, which mimics the heat flux of a medium with a low magma ocean viscosity:

$$k_{\mathrm{eff}} = F_{\mathrm{conv}} L / \Delta T, \tag{6}$$

where F_{conv} is the convective heat flux, L is the depth of the magma ocean and $\Delta T = T_p - T_s$, with the potential temperature T_p and the temperature T_s at the upper boundary of the magma ocean. In a silicate magma ocean this temperature corresponds to the silicate melt fraction of 50% and is equal to 1637 K. In a convecting core this is the temperature at the core–mantle boundary or at the upper boundary of the convecting part of the core. The latter is equal to or higher than the temperature of 1456 K, which corresponds to the iron melt fraction of 50%.

In the following we use the index i which is either Fe or Si to distinguish between a silicate magma ocean in the mantle and a convecting (part of the) core. The convective heat flux in the soft turbulence regime may be expressed as follows:

$$F_{\mathrm{conv},i} = 0.089 k_i (T_{p,i} - T_{s,i}) Ra_i^{1/3} / L_i, \tag{7}$$

where k_i is the thermal conductivity and Ra_i is the Rayleigh number (see e.g. Kraichnan, 1962). The Rayleigh number is computed from

$$Ra_i = \frac{\alpha_i g_i (T_{p,i} - T_{s,i}) \rho_i^2 c_{p,i} L_i^3}{k_i \eta_{l,i}} \tag{8}$$

where α_i is the thermal expansivity, g_i is the surface gravity of the respective convecting layer, ρ_i is the density, $c_{p,i}$ is the heat

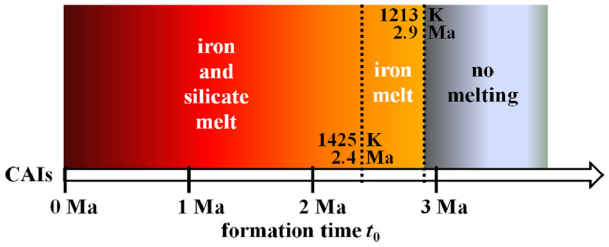


Fig. 1. Occurrence of iron and/or silicate melt for different formation times of Vesta assuming heat transport by conduction only and no differentiation.

capacity, and $\eta_{l,i}$ is the viscosity of the melt (here we assume a fixed value for simplicity, see Table 2).

Convection in the core is treated in a similar manner. Here, if the heat flux at the core–mantle boundary from the core into the mantle is positive and climbs above the adiabatic heat flux at the CMB, and the melt fraction in the core is above the RCMF, thermal convection is assumed to occur (Stevenson, 2003). This is achieved by solving Eqs. (6)–(8) using the parameters of the core.

The adiabatic heat flow at the radius $r = r_{\mathrm{CMB}}$ (corresponding to the core–mantle boundary) is computed from the equation

$$k_{\mathrm{c}}(dT/dr)_{\mathrm{ad,cmb}} = k_{\mathrm{c}}\alpha_{\mathrm{c}}T_{\mathrm{cmb}}g_{\mathrm{cmb}}/c_{\mathrm{pc}}, \tag{9}$$

where the index "c" denotes the core parameters, and the index "cmb" the parameters taken at the core–mantle boundary. Note that if only a part of the core is convecting, the respective parameters are not taken at the CMB, but at the upper boundary of the involved zone. For the parameters see Table 1 and Table 2.

We have tested the numerical code against existing codes in the literature. Details about these tests, the time discretisation and the chosen resolution can be found in the Supplementary Material.

3. Results

In first sample runs with purely conductive heat transport (thus, neglecting differentiation, heat transport by porous flow and convection in a magma ocean) we obtain a crude upper bound of the formation time $t_0 = 2.9$ Ma relative to the CAIs for the existence of a core – the solidus temperature of the silicate phase is exceeded in the centre of Vesta for formation times of up to 2.4 Ma and that of the metal phase for $t_0 \leqslant 2.9$ Ma relative to the CAIs (see Fig. 1). This upper boundary value can be refined if one considers differentiation.

Due to the effective radiogenic heating and the small surface-to-volume ratio, the temperature in the mantle can reach several thousand degrees. Mantle temperatures exceeding the liquidus temperature of 1850 K of silicates are obtained for formation times of $t_0 \leqslant 2$ Ma after the CAIs but are inconsistent with the conclusions of Mason (1962), Stolper (1975, 1977), Jones (1984) and Jones et al. (1996), who suggest that the eucrites were generated by no more than 25% partial melting of the source region (non-cumulate eucrite Sioux County, see Jones et al., 1996) and that 25% partial melting of the primordial mantle generated the crust. If one investigates the thermal evolution of Vesta without any additional cooling mechanisms except conduction, the only way to satisfy the physical constraints (e.g. 25% of silicate melting) is by assuming that Vesta formed at least 2 Ma after the CAIs. In this manner the thermal evolution of Vesta was investigated e.g. in Ghosh and McSween (1998). However, higher melt fractions could theoretically have been achieved in the source region after the extraction of melts which formed the eucrites.

Considering in a next step differentiation, partitioning of radioactive heat sources, heat transport by porous flow and convection, the thermo-chemical evolution differs significantly. Because ^{26}Al is an incompatible element and is saturated in the liquid silicate phase during the melting of the silicates, the migration of the silicate melt has notable effects on the thermal evolution if this process is considered. This is because the concentration of ^{26}Al becomes non-constant during and after the differentiation at different radii. Values of down to 0.003 have been suggested for the partitioning coefficient P, which controls the concentrations of ^{26}Al in the solid and in the liquid silicate phase (Kennedy et al., 1993; Pack and Palme, 2003). In the present study, we adopt the value $P = 0.02$ to avoid a possible bias of the results.

The following scenario applies to a formation time $t_0 < 1.0$ Ma after the CAIs (see Fig. 2). In the early stages of the differentiation, when the first silicate melt is produced, ^{26}Al-rich melt migrates towards the surface (at temperatures slightly above the silicate solidus of 1425 K) causing saturation of ^{26}Al in a shallow sub-surface layer. Simultaneously, the solid matrix, which is depleted in ^{26}Al, compacts downwards. Notice that the first melt produced is in fact metal melt due to the lower melting temperature of Fe–FeS in comparison to silicates but the metal melt fraction is too low to allow for significant melt migration – efficient migration of metal melt then occurs slightly later when the silicate differentiation begins (see also Neumann et al., 2012). In a shallow layer, temperature increases rapidly due to the strongly enhanced production of radiogenic heat (see Figs. 3, 4 and 5). Directly below a rigid undifferentiated shell the melt fraction rises up to the RCMF and convection starts in an approximately 1 km thick magma ocean. Close vicinity of the surface and effective cooling prevent the magma ocean from including the surface.

Directly above this superheated sub-surface layer and below the undifferentiated shell a region forms where silicate melt fractions lie below 50% and porous flow takes place. In this extremely thin boundary layer ^{26}Al saturated melt percolates to the surface. Convection and efficient cooling through the surface causes the potential temperature in the magma ocean to vary around 1637 K (at this temperature 50% of the material in the silicate magma ocean is molten and, thus, the RCMF is crossed) resulting in a fluctuation between convective and advective regimes. In the advective regime the ^{26}Al particles contained in the magma ocean migrate by porous flow into the boundary layer. This way, even more ^{26}Al rises to the surface from the boundary layer together with the erupting silicate melt. Still, due to the differentiation which takes place further below, additional ^{26}Al is transported into the magma ocean, which is subsequently heated above the critical temperature and switches again from the advective to the convective regime. Not all radioactive material leaves the mantle, nor does all of it reside at the surface. As soon as some portion of melt extrudes, it covers a part of the ^{26}Al-enriched crustal material. We assume that this material transports ^{26}Al into the boundary layer. This way material circulation between the surface and the boundary layer is established such that the critical temperature of 1637 K and, thus, a sub-surface magma ocean can be maintained right below the thin crust for as long as $O(10^4)$–$O(10^5)$ (see Fig. 5). This mechanism leads to a substantial reduction of heating throughout the body as the major part of the radioactive material (except ^{60}Fe) is involved in the material circulation between the crust and the upper mantle (here the crust is a solid basaltic carapace, the mantle is the layer with less than 1 vol% metal, the core is the central area with less than 1 vol% silicates). The sub-surface is the first completely differentiated part of the planetesimal. Simultaneously, the differentiation of the deeper layers proceeds. Thereby, the upper mantle is first cleared of the metal, then the rest of the mantle and the metal core form simultaneously.

The last stage of the silicate–metal differentiation is the formation of a distinct core–mantle boundary. After less than 0.3 Ma from the start of the melt migration, core formation is completed (e.g. for $t_0 = 0$ Vesta differentiates between 0.17 Ma and 0.33 Ma,

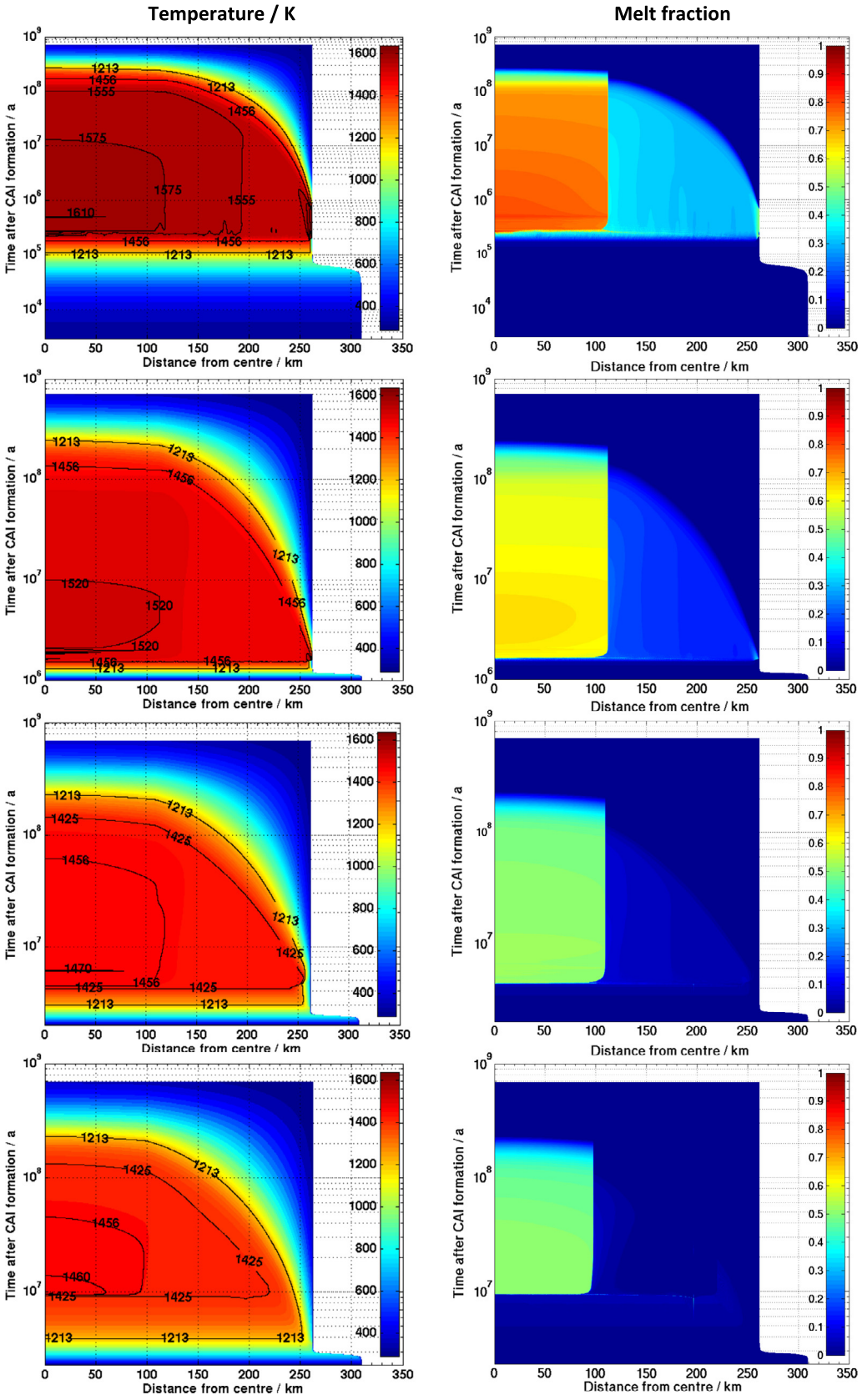


Fig. 2. Temporal evolution of the radial distribution of the interior temperature in K (left column) and melt fraction (right column) for different formation times relative to the CAIs. The panels correspond from top to bottom to $t_0 = 0, 1, 2$, and 2.3 Ma.

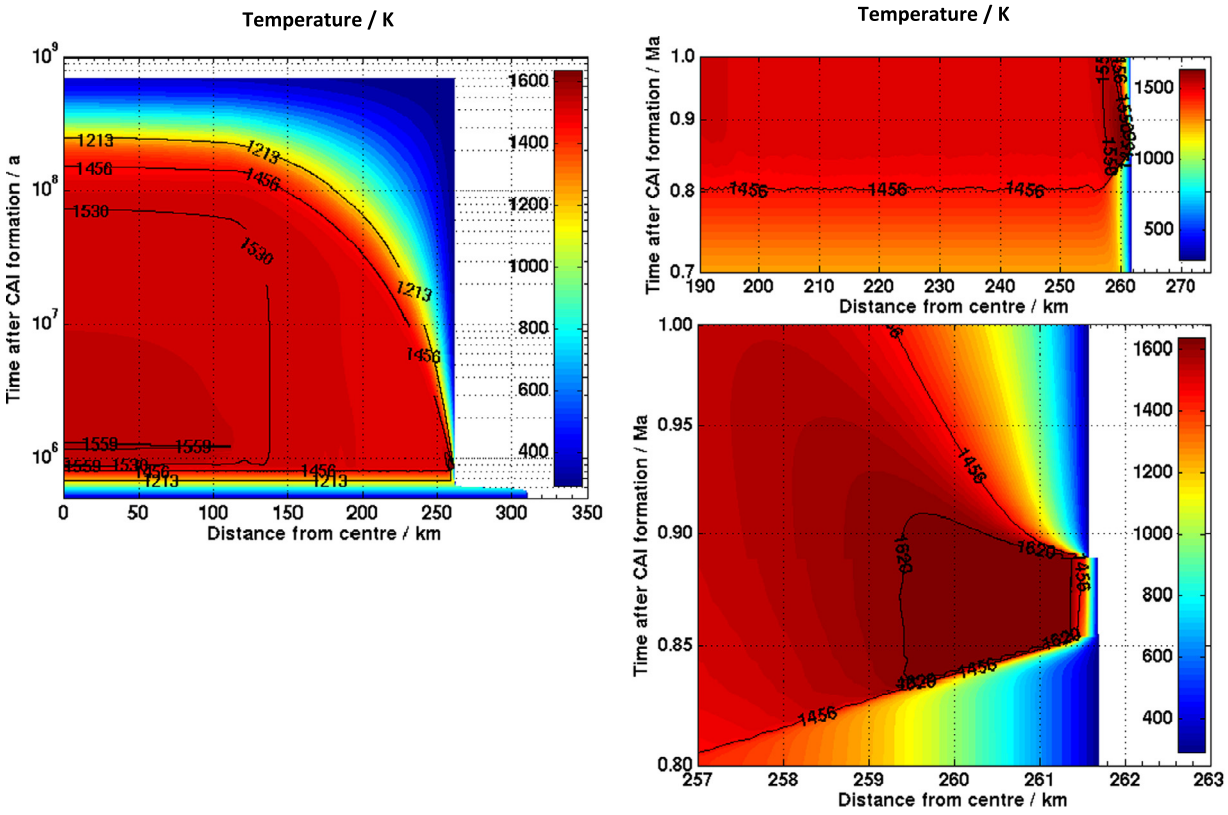


Fig. 3. Temperature (in K) ant two close-ups in the sub-surface magma ocean of a body which formed at $t_0 = 0.5$ Ma after the CAIs.

for $t_0 = 0.5$ Ma between 0.78 Ma and 1 Ma, and for $t_0 = 1$ Ma between 1.5 Ma and 1.72 Ma). As a consequence of the depletion in ^{26}Al of the mantle, the heat budget in almost the entire body is reduced to the heating from the core by ^{60}Fe decay only, and the heating of the mantle from above by the magma ocean. Whereas the melt fraction in the magma ocean is fixed at about 50%, the melt fractions in the deeper regions remain lower (<40%, see Figs. 2 and 4). The effects of the sub-surface magma ocean on the interior temperature wear off after approximately 1 Ma. After this time the temperature profile throughout the mantle establishes a negative gradient from the CMB towards the surface (cooling of the core).

For models with $t_0 > 1.0$ Ma almost no melt extrusion at the surface is observed although for $1.0 \leqslant t_0 < 2.0$ a superheated layer in the sub-surface forms. However, note that we do not consider crust formation via dykes. For $t_0 > 2.0$ Ma the effects of partitioning of ^{26}Al are negligible.

Regardless of the formation time, the melt fractions in the silicate mantle of Vesta remain below 40% (except in the shallow magma ocean), either due to the migration of the ^{26}Al enriched melt towards the surface, or as a result of the decline in the radiogenic heating with time. No deep (whole-mantle) magma ocean is observed. Due to the density contrast between the silicate melt and the solid silicate matrix, some melt percolation takes place during the cooling of the depleted mantle. This stops when the temperature decreases below the silicate solidus, e.g. at maximally 150 Ma after the CAIs above the CMB. Silicate melt is present at a depth of 50 km until 28 Ma and at the depth of 100 km until 97 Ma after the CAIs if Vesta forms contemporaneously with the CAIs (see Fig. 2).

In the core, as thermal convection takes place only if the heat flow at the CMB surpasses the adiabatic heat flow at the CMB, considerably higher temperatures than the critical temperature for the metal phase of 1456 K resulting in 50% partial melt are attained. Up to 75% of the core material manages to melt before convection starts. The temperature profile in the convecting core is regulated by the temperature of the lower mantle directly above the CMB (due to the difference between the potential temperature and the temperature at the upper boundary, which enters the effective thermal conductivity, see Eqs. (6)–(8)). The typical values of the Rayleigh number here are $Ra = \mathrm{O}(10^{19})$ and the effective thermal conductivity varies around $\mathrm{O}(10^6)$ W m^{-1} K^{-1}. The cooling through the CMB and the decline in the radiogenic heating puts the outer regions of the core into the advective regime below the RCMF of the metal phase. Subsequently the convecting inner part of the core becomes smaller through freezing of the outer regions until the convection ceases after ≈100 Ma after the formation of the body (note, however, that we do not consider crystal segregation in a Fe–Ni–FeS core – the implications of this process on the results are discussed below).

Fig. 6 shows the core radius (solid black line), the mantle thickness (dashed line) and the thickness of the undifferentiated outer layer (dotted line) as functions of the formation time. For $t_0 \leqslant 1.5$ Ma the core radius is approximately 111 km and is smaller for $1.5 < t_0 \leqslant 2.6$ Ma showing a sharp gradient between 2.3 Ma (97 km) and 2.6 Ma (≈1 km). The duration of the differentiation of rather small cores for the latter formation interval amounts to up to 170 Ma (as long as there is any melt). Formation prior to 1.5 Ma results in a complete or almost complete differentiation. At $t_0 = 2.7$–2.8 Ma no distinct core forms, although some increase in the metal concentration towards the centre can be observed as some melt migration below the radius of 216–188 km, respectively, takes place. No melt migration occurred for $t_0 = 2.9$ Ma. As for $t_0 > 2.3$ Ma the solidus temperature of silicates was not exceeded, differentiation for the bodies with later formation time is due to iron melt migration only (and is much slower). For $t_0 \leqslant 2.3$ Ma a silicate mantle forms and for $t_0 \geqslant 1.5$ Ma a thin primordial (porous) layer is retained at the surface, thickness of

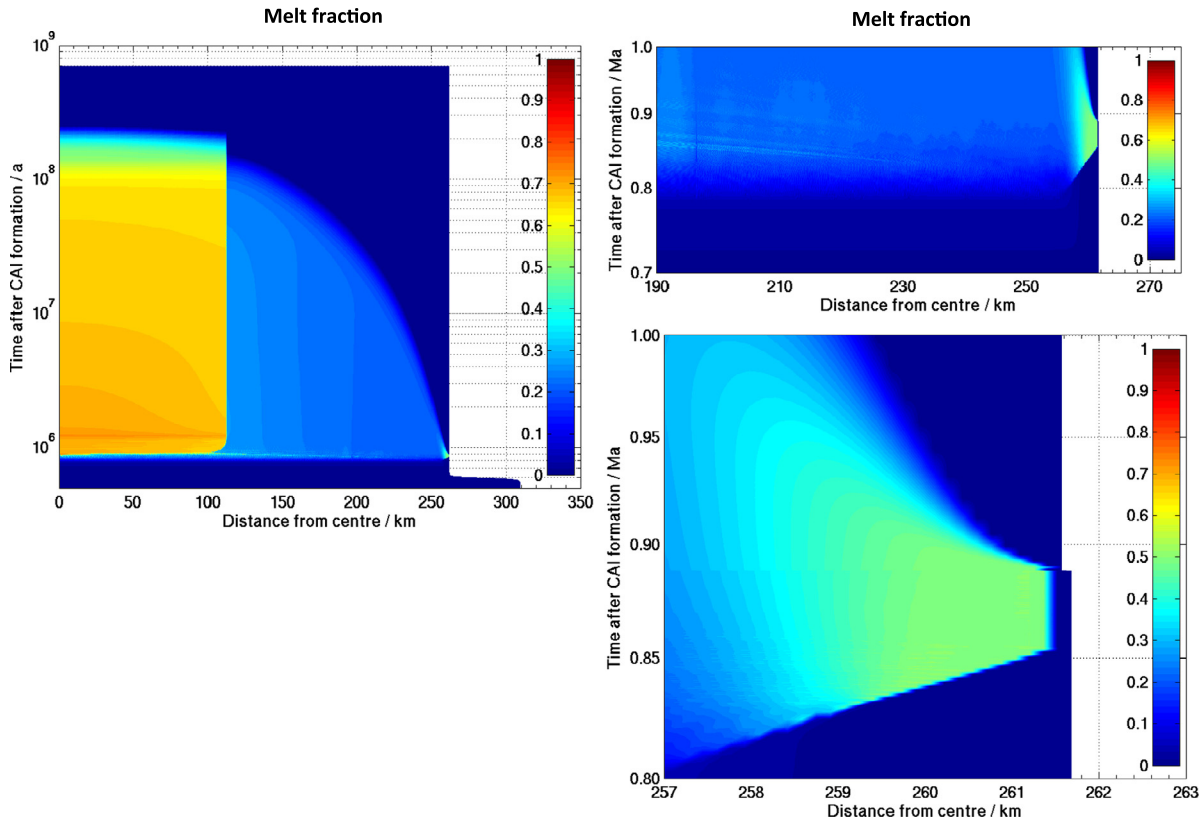


Fig. 4. Melt fraction and two close-ups in the sub-surface magma ocean of a body which formed at $t_0 = 0.5$ Ma after the CAIs.

the latter lying between 0.3 km at $t_0 = 1.5$ Ma and 2.8 km at $t_0 = 3$ Ma.

The present findings of a shallow magma ocean strongly depend on the migration velocity and here the most critical parameter is the silicate melt viscosity – the higher the viscosity the lower is the migration velocity and the more likely the formation of a global magma ocean and vice versa. In the present model, we have used a silicate melt viscosity of 1 Pa s. The viscosity of molten silicates varies from 0.001 to 1000 Pa s (Moskovitz and Gaidos, 2011), however, basaltic melts derived from chondritic precursors have silica contents generally $\lesssim$50% (Mittlefehldt et al., 1998) and viscosities of $\approx$1–100 Pa s (Giordano et al., 2008). Further tests with melt viscosities of 10 and 100 Pa s show that an increase of the silicate melt viscosity results in lower melt migration velocities, thicker sub-surface magma ocean (e.g. $\approx$10 km for 10 Pa s in comparison to 1 km for 1 Pa s) and slower silicate separation. The cooling of the magma ocean below the RCMF is prolonged to 1 Ma and the layer is entirely crystallised after 3 Ma. Higher temperatures are obtained in the mantle and in the core, because of the somewhat prolonged radiogenic heating by the slow migrating ^{26}Al. In the extreme case of 100 Pa s, the magma ocean even extends to the depth of $\approx$100 km. The rest of the mantle reaches melt fractions close to the RCMF and the iron-rich core, the silicate mantle and the crust from almost simultaneously. Apart from the thickness of the sub-surface magma ocean and the melt fractions (temperatures) in the body below, the most important effects described in the general scenario (fast silicate–metal differentiation, extrusion of ^{26}Al, melt fractions in the magma ocean remain close to the threshold of 50%, etc.) are still valid.

The amount of heating by ^{60}Fe is connected to the initial ratio $[^{60}\mathrm{Fe}/^{56}\mathrm{Fe}]_0 = 1.6 \cdot 10^{-6}$ adopted in our calculations. To test the influence of this parameter on the results we performed test runs assuming values of $1.0 \cdot 10^{-7}$, $1.0 \cdot 10^{-8}$ and $1.0 \cdot 10^{-9}$. The effect on the occurrence and evolution of the magma ocean is negligible, because the abundance of the major heat source ^{26}Al remains constant. Furthermore, the melt fractions in the core and in the lower mantle decrease by less than 10% with the falling initial abundance of ^{60}Fe. This decreases the duration of the thermal convection in the core slightly by less than 10 Ma.

In the following, we have also examined the influence of the partitioning of ^{26}Al on the thermo-chemical evolution of Vesta by considering $P = 1$ (no partitioning) to better compare the results with models that neglect partitioning. The duration of the differentiation is only slightly shorter than for $P = 0.02$, but the order of crust-mantle and core–mantle differentiation differs. As in the case of $P = 0.02$, first silicate and iron melt migration is observed at approximately 50 km depth and not in the centre – due to increasing gravity with radius and almost equal melt fraction as in the centre (owed to a flat temperature profile). Simultaneously, the silicate mantle grows down- and upwards from the region where the differentiation started, and the metal core grows upwards from the centre. In the last stage of the iron–silicate differentiation, a clear CMB is established. After core formation, a magma ocean starts to form somewhere in the mid-mantle. The melt from the boundary layer above the magma ocean is not able to percolate through the chondritic carapace and to form a basaltic crust. Even in the hottest scenario with $t_0 = 0$ Ma an undifferentiated (although compacted) primordial crust of $\approx$1 km thickness remains.

4. Discussion and conclusions

Our simulations imply that no whole-mantle silicate magma ocean formed in the mantle of Vesta – percolation of silicate melt and the depletion of ^{26}Al in the mantle is faster than the heating of the mantle by the radioactive elements, as also suggested by Moskovitz and Gaidos (2011) for smaller bodies. The entire silicate material did not exceed the critical temperature of approximately 1637 K (and the corresponding threshold melt fraction of 50%) and

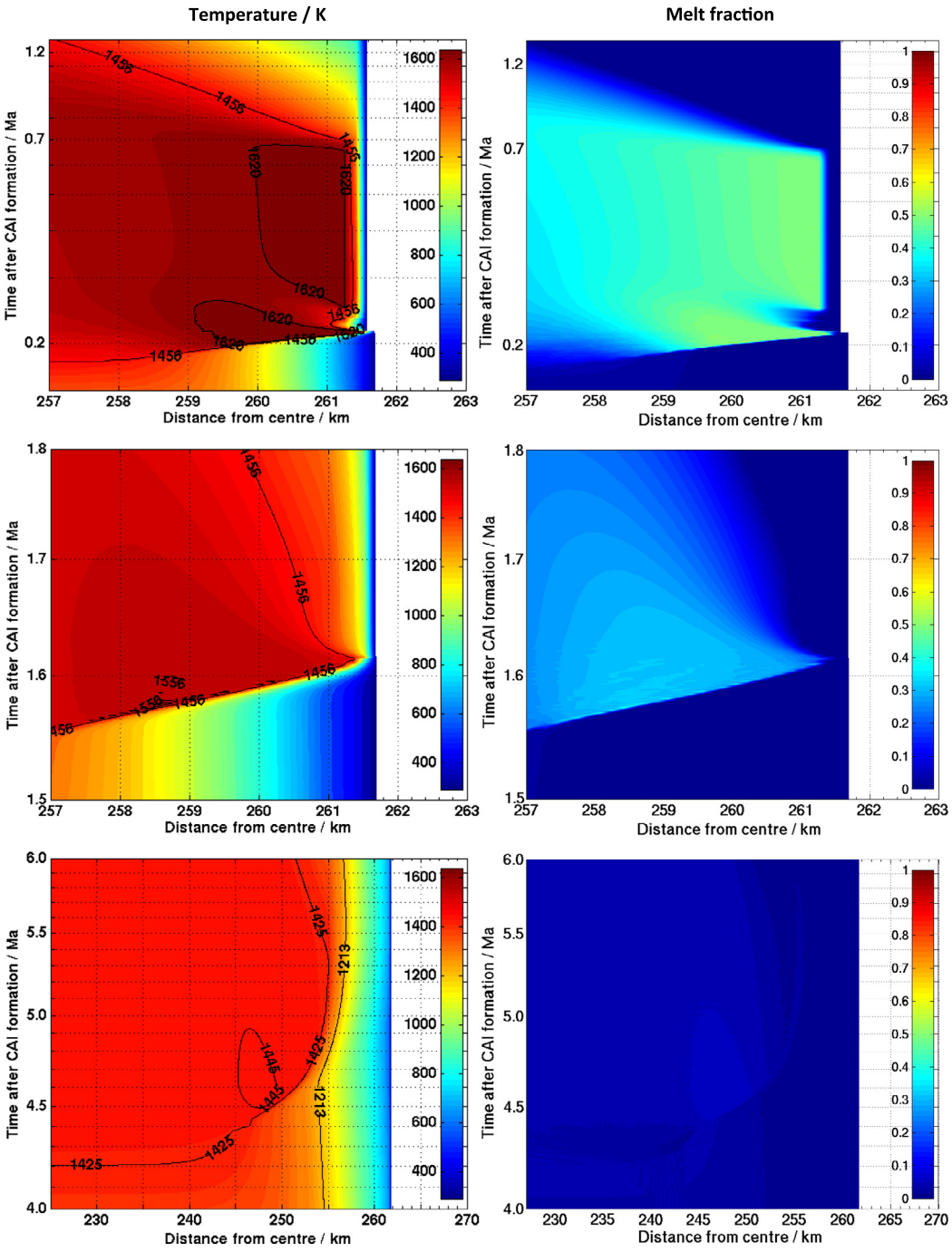


Fig. 5. Close-ups of the sub-surface magma ocean or the super-heated sub-surface region for different formation times: $t_0 = 0$ Ma (upper panels), 1 Ma (middle panels), 2 Ma (lower panels). Left column: Temperature in K. Right column: Melt fraction.

for the most part the melt fractions in the mantle remained below 40%. Even in the thin sub-surface magma ocean this critical temperature is exceeded by only a few degrees. The critical temperature varies, in general, with the assumptions about the melting behaviour of the silicate material (we assumed linear melting between the solidus and the liquidus of the silicates). Furthermore, the adopted value of the RCMF of 0.5 can be debated, as liquid-state convection may occur already at lower melt fractions (even values of down to 20% have been suggested, see e.g. Arzi, 1978; Taylor, 1992; Lejeune and Richet, 1995; Scott and Kohlstedt, 2006). Assuming a smaller threshold value of the RCMF for the onset of convection would result in the fixation of the temperature in the convecting zone at the temperature corresponding to the associated melt fraction. Thus, the source regions of the melt which formed the HED meteorites most likely never exceeded 20 to 50% melting and the corresponding temperature.

4.1. Interior evolution of Vesta

Based on our findings we suggest the evolution of the interior of Vesta shown in Fig. 7, top row.

After the initial accretion phase (which is approximated here by instantaneous formation at the time t_0), the radiogenic heating induces compaction of the porous material and the associated bulk volume decrease. Having a flat temperature profile with a sharp gradient in a thin outer porous layer, melt is produced even

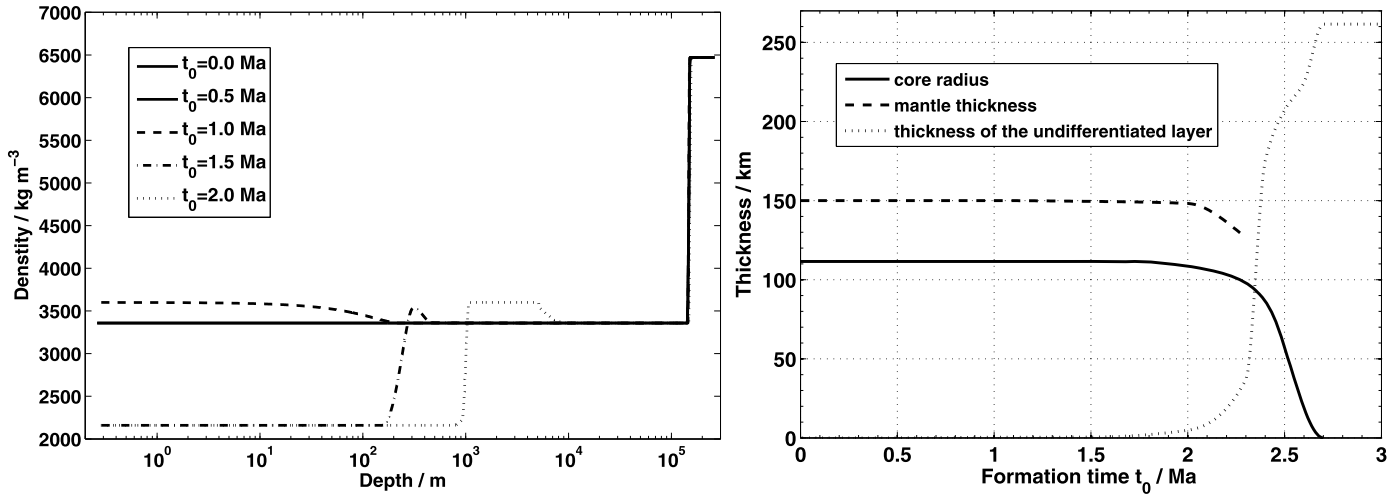


Fig. 6. Left panel: Density versus depth for different formation times after the cooling below the solidus temperature of the metal phase. Right panel: Core radius, mantle thickness and the thickness of the undifferentiated layer for different formation times. Note that for $t_0 \geqslant 2.3$ Ma no clear mantle forms.

in shallow regions. Upon the onset of the differentiation ^{26}Al is enriched in the outer 2–15 km of the body and the high temperatures and high degree of melting close to the surface cause compaction of the chondritic crust, the differentiation of the shallow layers and the melt eruptions at the surface. For viscosities of silicate melt between 1 and 10 Pa s a shallow magma ocean with a thickness of 1 to 10 km forms. The magma ocean cools rapidly within O(10^4)–O(10^6) a and its thickness, as well as the time scale of solidification, increases with increasing silicate melt viscosity.

Rapid cooling of the magma ocean on the HED parent body within 2–3 Ma has been suggested as a consequence of ^{26}Mg variations among diogenites and eucrites (Schiller et al., 2011). However, Schiller et al. (2011) concluded that such a rapid cooling can occur only in asteroids with radii smaller than 100 km implying that Vesta is not the parent body of the HEDs. In contrast, our results admit both the size of Vesta and high cooling rates.

While ^{26}Al is transported to the surface, the differentiation proceeds downwards: a basaltic crust, a purely silicate upper mantle and an iron-rich core form, with the completion of the mantle and a clear CMB, subsequently. The observed basaltic surface of Vesta (e.g. McSween et al., 2013) favours formation times $t_0 < 1$ Ma, as in those cases the silicate melt is able to penetrate the outermost layer via porous flow and thereby to cover the entire surface. This correlates with the lack of a large amount of relict undifferentiated material (e.g. De Sanctis et al., 2012) and the presence of basaltic crust but lack of distinct volcanic regions on Vesta (Jaumann et al., 2012). Volcanism caused by melt transport via dykes may violate these findings. Furthermore, the ^{26}Mg composition of the most primitive diogenites requires onset of the magma ocean crystallisation within $0.6^{-0.4}_{+0.5}$ Ma after CAIs (Schiller et al., 2011), consistent with the formation times of $t_0 < 1$ Ma.

The silicate–metal differentiation is rapid and, in general, completed within 0.3 Ma after onset of melting; nevertheless, its initiation succeeds early silicate differentiation (crust formation). This sequence is different to what is generally assumed for planetesimals from chronological records, i.e., core formation precedes crust formation (e.g. Kleine et al., 2009). To reverse the differentiation sequence either metal segregation needs to be accelerated or silicate segregation slowed down. Metal segregation is enhanced, for instance, for a high concentration of FeS close to the eutectic (Neumann et al., 2012) or a lower viscosity of iron melt. In the present study, we have assumed an L-chondritic composition of Vesta with only 5 wt% of FeS and a melt viscosity of 10^{-2} Pa s. However, higher concentrations of FeS in Vesta have been also suggested with values of ∼10 wt%, corresponding to a Vesta-like body composed of 70 wt% ordinary chondrite and 30 wt% carbonaceous chondrite (Boesenberg and Delaney, 1997). Furthermore, experiments show a variation of the viscosity of iron-rich melt between 10^{-3} and 10^{-2} Pa s (Dobson et al., 2000; Assael et al., 2006) and we took the standard value of 10^{-2} Pa s used in the literature.

Although we cannot discriminate between the composition of the various silicate liquid and solid phases in our model, we speculate that the first partial melt reaching the surface produced non-cumulate eucrites. The cumulate eucrites and the diogenites are suggested to have formed as a consequence of the crystallising sub-surface magma ocean. The latter has an olivine-poor composition as it contains mainly partial melt that is transported upward from the mantle below. In addition, at the same time the original solid matrix in the magma ocean region is pushed down and replaced by crystallising partial melt from the lower mantle. Thus, in our scenario the non-cumulate eucrites form prior to the cumulate eucrites and diogenites. This order of formation is supported by the internal ^{26}Al–^{26}Mg isochrones obtained by Hublet et al. (2013), who infer younger ages for the diogenites compared to those of the eucrites, and younger ages for the cumulate eucrites compared to the non-cumulate ones. Although our physical model supports the early partial melt origin of the non-cumulate eucrites, it should be noted that petrological studies favour their origin from magma fractionation (see e.g. Righter and Drake, 1997; Mandler and Elkins-Tanton, 2013). It needs to be tested in future studies whether our proposed scenario is also compatible with the petrology of the HEDs as this is out of the scope of the present paper.

It should be noted, though, that silicate melting and melt migration is ongoing for up to 150 Ma and, thus, much longer than silicate–metal separation. However, the upper melting front moves continuously to greater depth. Partial melting generated later than the early eucritic crust is not able to rise to the surface and will remain in the lower crust or mantle.

High values of the silicate melt viscosity between 10 to 100 Pa s suggest that the subsurface magma ocean can even reach a thickness up to 100 km. A sub-surface magma ocean with a thickness of a few tens of kilometres would in fact be more consistent with the assumption of Vesta's crust having an average thickness of 35–85 km with an upper eucritic and a lower orthopyroxene-rich layer (McSween et al., 2013).

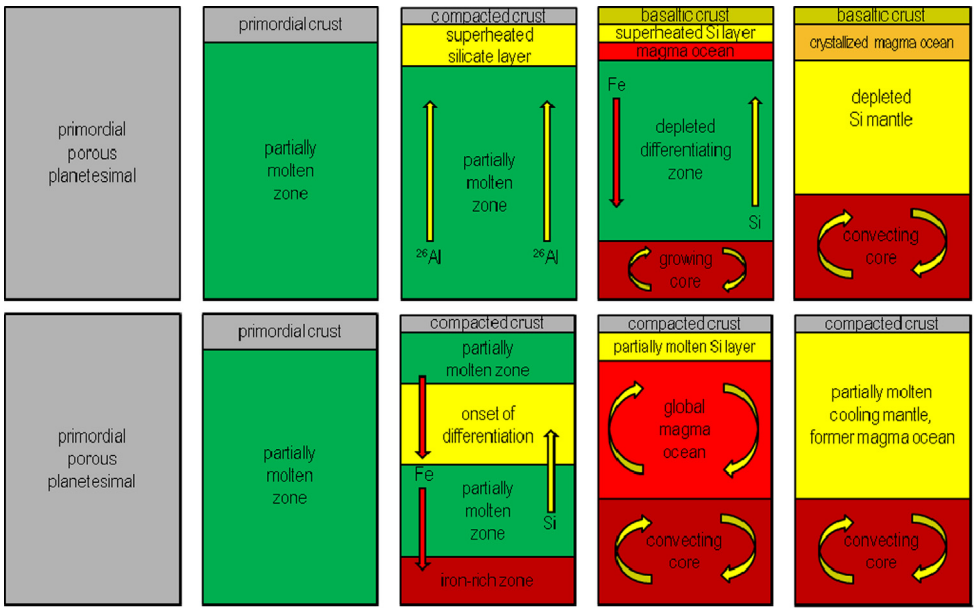


Fig. 7. Top row: Evolution path of the interior assuming partitioning of ^{26}Al. Bottom row: Evolution path of the interior neglecting partitioning of ^{26}Al.

Our results suggest that no global magma ocean down to the core mantle boundary forms because the silicate melt including ^{26}Al is transported toward the surface. This result is, in particular, valid for a RCMF of 0.5. For smaller values of the critical melt fraction – that determines the change in the rheological behaviour and defines the existence of a magma ocean from the physical perspective (low viscosity) – the critical temperature is reached faster. However, in our approach we have neglected the composition of the various silicate liquid and solid phases and, thereby, also the variation in the melting temperature with composition. Depleting the mantle in crustal components due to magma migration results in higher solidus temperatures of the residual material and, thus, reduced subsequent partial melting in the lower mantle. In contrast, in the shallow magma ocean, which accumulates partial melt of the lower mantle that has a lower liquidus temperature than the primordial material, a higher degree of melting is possible (than calculated in our approach). Thus, a more detailed study that also considers the individual silicate phases may strengthen our finding of a shallow sub-surface and no global magma ocean on Vesta.

The iron-rich core starts to convect by thermal buoyancy already during its formation. Convection and cooling of the core through the depleted mantle is then maintained for up to O(10^8) a. It should be noted, though, that the core was – like the mantle – not entirely melted and the melt fraction stayed below 75%. Thus, an early dynamo is not by thermal convection only, i.e. a purely early thermal dynamo is not likely in Vesta. Chemical convection due to freezing processes in the core may play a substantial role for the magnetic field generation in planetesimals (Nimmo, 2009). The freezing process and chemical convection have been simplified here and need further studies.

The less realistic evolution path from Fig. 7, bottom row, results in the formation of a convecting whole-mantle magma ocean. Here, the distribution of ^{26}Al is homogeneous throughout the silicate phase (both solid and liquid). Note that by contrast to previous thermo-chemical evolution models considering a magma ocean scenario (e.g. Gupta and Sahijpal, 2010), the differentiation does not start in the centre, but in the upper mantle. Furthermore, the silicate melt from the mantle is not able to penetrate the chondritic crust via porous flow, thus, likely no basalts form at the surface and the differentiation is not complete. However, ongoing impacts, presence of volatiles, and excess pressure in the interior due to melting could act in favour of melt ascent via cracks to produce a basaltic crust (Wilson and Keil, 2012). The chondritic crust could be also carved off by impacts exposing the differentiated silicate layers although one would expect relicts of undifferentiated material that have not been observed (e.g. De Sanctis et al., 2012).

4.2. Comparison to previous thermo-chemical evolution models

Our results suggest that most previous thermo-chemical evolution models for Vesta tend to overestimate the temperature increase in the interior and therefore the amount of partial melting (Righter and Drake, 1997; Ghosh and McSween, 1998; Drake, 2001; Gupta and Sahijpal, 2010). Those models either neglect efficient heat transport by the partitioning of ^{26}Al into the silicate melt or convection in a magma ocean.

The convective cooling method used by Hevey and Sanders (2006) for small planetesimals $<$100 km in radius (increase of k by three orders of magnitude for melt fractions $\geqslant$50%) has been also adopted by Gupta and Sahijpal (2010) for Vesta (a steady increase of the thermal diffusivity between the melt fractions of 50% and 100% by three orders of magnitude).

Thus, a maximal value of $\approx$3300 W m^{-1} K^{-1} has been used for effective thermal conductivity by Gupta and Sahijpal (2010). The effective thermal conductivity, however, varies with the cube root of gravity times the depth of the convecting zone (Eqs. (6)–(8)). Hence, the larger the radius and/or the convecting zone, the larger is k_{eff}. In our simulations values of O(10^6) W m^{-1} K^{-1} can be obtained for $\Delta T = \mathrm{O}(1)$ K (the difference between the potential temperature and the temperature at the upper boundary of the convecting zone). This explains the much higher temperatures of up to 2000 K obtained by Gupta and Sahijpal (2010). Our model in which the partitioning of ^{26}Al is neglected as in Gupta and Sahijpal (2010) show a global magma ocean but still the temperatures do not exceed significantly the threshold melt fraction of 50% due to efficient cooling.

Our results further imply that previous thermal evolution models for planetesimals to explain the magnetic field generation in their iron-rich cores such as presented in e.g. Elkins-Tanton et al. (2011), Elkins-Tanton (2012) and Sterenborg and Crowley (2013) have to be considered with care although they consider efficient cooling by convection. These models start with a differentiated

structure and further neglect volcanic heat transport and partitioning of ^{26}Al. Thereby, thermal convection in the core and magnetic field generation is initiated due to the efficient cooling of the magma ocean after an initial phase of heating by the radioactive heat sources. It can be shown in our models that when considering the entire differentiation process, i.e. silicate–metal and silicate–silicate differentiation, the temperature profile after core formation shows a temperature profile increasing toward the surface and inhibiting convection. A whole-mantle magma ocean does not form and, as a consequence, the lower mantle cools by conduction only. Nevertheless, the core heat flow is higher than the heat flow along the core adiabat, suggesting thermal convection in the core for about 100 Ma. This finding is in contrast to the assumption of Sterenborg and Crowley (2013), who argue that thermal convection in the core is inhibited when the mantle cools by conduction using a simple model of conductive cooling. It should be noted, though, that the strength of thermal core convection in our model is likely not sufficient to generate a dynamo, i.e. is the magnetic Reynolds number is lower than about O(10–100) (e.g. Christensen et al., 2009). However, we do not explicitly differentiate between the iron–nickel system and lighter elements in the core (such as those contained in the Fe–FeS system). This means that our model does not allow freezing and growth of a solid inner core and the establishment of a liquid outer core due to the exclusion of light elements from the crystal structure, as well as the latent heat release at the inner core boundary. Thus, chemically driven convection (Stevenson, 2003; Nimmo, 2009) and its contribution to the magnetic field are neglected.

4.3. Solid-state convection

As mentioned further above, the solid-state plastic deformation (other than compaction due to sintering, see e.g. Tkalcec et al., 2013) for melt fractions below 50% has been neglected in the present study. First, the conditions for solid-state convection are fulfilled several million years after the solidification of the shallow magma ocean. Before that time, the temperatures in the upper mantle (magma ocean region) are higher than in the lower mantle and thermal convection is suppressed. Second, the maximal Rayleigh number that we obtain when the conditions are favourable for convection is estimated to be ≈5500, which exceeds the critical Rayleigh number of 1000 (e.g. Schubert et al., 2001) required for convection only moderately. Because this type of convection takes place after the magma ocean has vanished, it has no effect on the main results presented in the paper. However, the latest time of occurrence of partial melt in the mantle and the time scale of the convection in the core could change slightly.

4.4. Melt ascent through a porous crust and formation of dykes

Our results suggest the formation of a basaltic crust by porous flow. It has been argued, however, that melt ascent through a porous chondritic crust is unlikely due to the lack of the positive density contrast (e.g. Elkins-Tanton et al., 2011; Fu and Elkins-Tanton, 2014). In our simulations of Vesta the porous chondritic material in the sub-surface compacts readily due to hot pressing if exposed to the temperatures far below the silicate solidus of ≈1425 K. Before any silicate melt is produced, the thickness of the porous layer is ≈300 m. Once migrating silicate melt accumulates ^{26}Al in the sub-surface, additional heating leads to the closure of the remaining pores, except in a thin surface layer (≈100 m). This result is supported by the numerical simulations of Henke et al. (2012, 2013). Consequently, the density contrast between the melt and the matrix is still maintained. This ≈100 m thick porous layer does not represent a barrier for buoyant rising melt (see Fig. 6 and discussion on the dyke propagation in the Supplementary Material). However, to model the compaction we use the material parameters in Schwenn and Goetze (1978) that result from experiments of pure olivine powders. Since an L-chondritic composition contains further minerals, we do not exclude that parameters like the activation energy or grain size can vary. A higher value of the activation energy would possibly imply a thicker outer porous layer, which may act against the rise of the melt by porous flow only (see the arguments in Fu and Elkins-Tanton, 2014).

On the other hand, compacted chondritic material at the surface could have been fractured due to impacts. However, this should not hinder melt ascension, but would rather favour the extraction of melt via dykes. Also, large pressures can be generated in the sub-surface for small degrees of melting (e.g. a pressure of 0.1 GPa for a melt fraction of 0.2, see Wilson and Keil, 2012), and eruptions would occur when the excess pressure due to the accumulation of magma in the sub-regolith reservoirs exceeds the tensile stress of the overlying rock (Wilson and Keil, 2012). The presence of small amounts of volatiles reduces the magma density and increases the excess pressure. Note, though, that to keep the fractures open and to allow efficient cooling by the silicate melt transport directly from the deep mantle to the surface, Vesta may be a boundary case due to its small size. Instead, magma would first accumulate in sills or magma layers at the base of the upper thermal boundary layer before eruption (Wilson and Keil, 2012).

Efficient melt migration via dykes – if possible – suggests even faster cooling of the interior than via porous flow and strengthens the result presented here. Consequently, faster cooling of the mantle and a shorter time span of the convection in the core are expected.

Acknowledgements

We thank R.R. Fu and one anonymous reviewer for the constructive and helpful comments on the paper. This work was supported by the Deutsche Forschungsgemeinschaft (DFG) Priority Programme 1385 “The First 10 Million Years of the Solar System – a Planetary Materials Approach” (grant BR 1602/6-2) and by the Helmholtz Association through the research alliance “Planetary Evolution and Life”.

Appendix A. Supplementary material

Supplementary material related to this article can be found online at http://dx.doi.org/10.1016/j.epsl.2014.03.033.

References

Arzi, A.A., 1978. Critical phenomena in the rheology of partially melted rocks. Tectonophysics 44 (1–4), 173–184.
Assael, M.J., 10 colleagues, 2006. Reference data for the density and viscosity of liquid aluminum and liquid iron. J. Phys. Chem. Ref. Data 35, 285.
Barrat, J.A., Yamaguchi, A., Benoit, M., Cotten, J., Bohn, M., 2008. Geochemistry of diogenites: still more diversity in their parental melts. Meteorit. Planet. Sci. 43 (11), 1759–1775.
Beck, A.W., McSween, H.Y., 2010. Diogenites as polymict breccias composed of orthopyroxenite and harzburgite. Meteorit. Planet. Sci. 45 (5), 850–872.
Best, M.G., 2002. Igneous and Metamorphic Petrology, 2nd edition. Wiley-Blackwell.
Boesenberg, J.S., Delaney, J.S., 1997. A model composition of the basaltic achondrite planetoid. Geochim. Cosmochim. Acta 61, 3205–3225.
Cameron, A.G.W., 1993. Nucleosynthesis and star formation. In: Levy, E.H., Lunine, J.I. (Eds.), Protostars and Planets III. Univ. of Arizona Press, Tucson, p. 47.
Christensen, U., Olson, P., Glatzmaier, G.A., 2009. Numerical modeling of the geodynamo: a systematic parameter study. Geophys. J. Int. 138, 393–409.
Delaney, J.S., 1995. 4 Vesta: a thick-skinned parent for basaltic achondrites. In: Lunar and Planetary Science XXVI, pp. 329–330 (abstract).
De Sanctis, M.C., 22 colleagues, 2012. Spectroscopic characterization of mineralogy and its diversity across Vesta. Science 336, 697.
De Sanctis, M.C., 17 colleagues, Dawn Team, 2013. Olivine on Vesta: clues for the interior. In: European Planetary Science Congress 2013. EPSC2013-437 (abstract).

Dobson, D.P., 8 colleagues, 2000. In situ measurement of viscosity of liquids in the Fe–FeS system at high pressures and temperatures. Am. Mineral. 85, 11–12, 1838–1842.
Drake, M.J., 2001. The eucrite/Vesta story. Meteorit. Planet. Sci. 36 (4), 501–513.
Elkins-Tanton, L.T., 2012. Magma oceans in the inner solar system. Annu. Rev. Earth Planet. Sci. 40, 113–139.
Elkins-Tanton, L.T., Weiss, B.P., Zuber, M.T., 2011. Chondrites as samples of differentiated planetesimals. Earth Planet. Sci. Lett. 305, 1–10.
Fu, R.R., 7 colleagues, 2012a. An ancient core dynamo in asteroid Vesta. Science 338, 238–241.
Fu, R.R., Weiss, B.P., Li, L., Suavet, C., Gattacceca, J., Lima, E.A., 2012b. Magnetic fields on 4 Vesta as recorded in two eucrites. In: Lunar and Planetary Science XLIII, p. 1496 (abstract).
Fu, R.R., Elkins-Tanton, L.T., 2014. The fate of magmas in planetesimals and the retention of primitive chondritic crusts. Earth Planet. Sci. Lett. 290, 128–137.
Ghosh, A., McSween Jr., H.Y., 1998. A thermal model for the differentiation of asteroid 4 Vesta, based on radiogenic heating. Icarus 134, 187–206.
Giordano, D., Russell, J.K., Dingwell, D.B., 2008. Viscosity of magmatic liquids: a model. Earth Planet. Sci. Lett. 271, 123–134.
Golabek, G.J., Keller, T., Gerya, T.V., Zhu, G., Tackley, P.J., Connolly, J.A.D., 2011. Origin of the Martian dichotomy and Tharsis from a giant impact causing massive magmatism. Icarus 215, 346–357.
Gupta, G., Sahijpal, S., 2010. Differentiation of Vesta and the parent bodies of other achondrites. J. Geophys. Res. 115, E08001.
Greenwood, R.C., Franchi, I.A., Jambon, A., Buchanan, P.C., 2005. Widespread magma oceans on asteroidal bodies in the early Solar System. Nature 435, 916–918.
Henke, S., Gail, H.-P., Trieloff, M., Schwarz, W.H., Kleine, T., 2012. Thermal evolution and sintering of chondritic planetesimals. Astron. Astrophys. 537, A45.
Henke, S., Gail, H.-P., Trieloff, M., Schwarz, W.H., 2013. Thermal evolution model for the H chondrite asteroid – instantaneous formation versus protracted accretion. Icarus 226, 212–228.
Hevey, P.J., Sanders, I.S., 2006. A model for planetesimal meltdown by ^{26}Al and its implications for meteorite parent bodies. Meteorit. Planet. Sci. 41, 95–106.
Hublet, G., Debaille, V., Wimpenny, J., Yin, Q.-Z., 2013. Geological history of 4-Vesta: ^{26}Al–^{26}Mg dating on eucrites and diogenites. Mineral. Mag. 77 (5), 1343.
Ikeda, Y., Takeda, H., 1985. A model for the origin of basaltic achondrites based on the Yamato 7308 howardite. J. Geophys. Res. 90, C649–C663.
Ivanov, B.A., Melosh, H.J., 2013. Two-dimensional numerical modeling of the Rheasilvia impact formation. J. Geophys. Res., Planets 118 (7), 1545–1557.
Jarosevich, E., 1990. Chemical analyses of meteorites: a compilation of stony and iron meteorite analyses. Meteoritics 25, 323–337.
Jaumann, R., 42 colleagues, 2012. Vesta's shape and morphology. Science 336, 6082, 687.
Jones, J.H., 1984. The composition of the mantle of the eucrite parent body and the origin of eucrites. Geochim. Cosmochim. Acta 48, 641–648.
Jones, J.H., Mittlefehldt, D.W., Jurewicz, A.J.G., Lauer, H.V., Hanson, B.Z., Paslick, C.R., McKay, G.A., 1996. The origin of eucrites: an experimental perspective. In: Mittlefehldt, D.W., Papike, J.J. (Eds.), Workshop on Igneous Asteroids: Focus on Vesta and the HED Meteorites. Lunar and Planetary Institute, Houston, 15 pp.
Jutzi, M., Asphaug, E., 2011. Mega-ejecta on asteroid Vesta. Geophys. Res. Lett. 38, L01102.
Kennedy, A., Lofgren, G., Wasserburg, G., 1993. An experimental study of trace element partitioning between olivine, orthopyroxene, and melt in chondrules: equilibrium values and kinetic effects. Earth Planet. Sci. Lett. 115, 177–195.
Kleine, T., 8 colleagues, 2009. Hf-W chronology of the accretion and early evolution of asteroids and terrestrial planets. Geochim. Cosmochim. Acta 73 (17), 5150–5188.
Kraichnan, R.H., 1962. Turbulent thermal convection at arbitrary Prandtl number. Phys. Fluids 5 (11), 1374–1389.
Lejeune, A.-M., Richet, P., 1995. Rheology of crystal-bearing silicate melts: an experimental study at high viscosities. J. Geophys. Res., Solid Earth (1978–2012) 100, 4215–4229, B3.
Mandler, B.E., Elkins-Tanton, L.T., 2013. The origin of eucrites, diogenites, and olivine diogenites: magma ocean crystallization and shallow magma chamber processes on Vesta. Meteorit. Planet. Sci. 48 (11), 2333–2349.
Marsh, B.D., 1988. Crystal capture, sorting, and retention in convecting magma. Geol. Soc. Am. Bull. 100 (11), 1720–1737.
Mason, B., 1962. Meteorites. Wiley, New York.
McSween, H.Y., 21 colleagues, 2013. Composition of the Rheasilvia basin, a window into Vesta's interior. J. Geophys. Res., Planets 118 (2), 335–346.
Mittlefehldt, D., McCoy, T., Goodrich, C., Kracher, A., 1998. Non-chondritic meteorites from asteroidal bodies. In: Papike, J. (Ed.), Planetary Materials. In: Reviews in Mineralogy, vol. 36. Mineralogical Society of America, Washington, D.C., pp. 4.01–4.195.
Moskovitz, N., Gaidos, E., 2011. Differentiation of planetesimals and the thermal consequences of melt migration. Meteorit. Planet. Sci. 46 (6), 903–918.
Neumann, W., Breuer, D., Spohn, T., 2012. Differentiation and core formation in accreting planetesimals. Astron. Astrophys. 543 (A141), 1–21.
Neumann, W., Breuer, D., Spohn, T., 2013. The thermo-chemical evolution of asteroid 21 Lutetia. Icarus 224, 126–143.
Nimmo, F., 2009. Energetics of asteroid dynamos and the role of compositional convection. Geophys. Res. Lett. 36, L10201.
Ogliore, R.C., Huss, G.R., Nagashima, K., 2011. Ratio estimation in SIMS analysis. Nucl. Instrum. Methods Phys. Res., Sect. B, Beam Interact. Mater. Atoms 269, 1910–1918.
Pack, A., Palme, H., 2003. Partitioning of Ca and Al between forsterite and silicate melt in dynamic systems with implications for the origin of Ca, Al-rich forsterites in primitive meteorites. Meteorit. Planet. Sci. 38, 1263–1281.
Palme, H., Rammensee, W., 1981. The cosmic abundance of molybdenum. Earth Planet. Sci. Lett. 55, 356–362.
Prettyman, T.H., 19 colleagues, 2012. Elemental mapping by Dawn reveals exogenic H in Vesta's regolith. Science 338, 242–246.
Raymond, C.A., 9 colleagues, 2012. Geophysical exploration of Vesta. In: Lunar and Planetary Science XLIII, p. 1007 (abstract).
Righter, K., Drake, M.J., 1997. A magma ocean on Vesta: core formation and petrogenesis of eucrites and diogenites. Meteorit. Planet. Sci. 32 (6), 929–944.
Rivoldini, A., Van Hoolst, T., Verhoeven, O., Mocquet, A., Dehant, V., 2011. Geodesy constraints on the interior structure and composition of Mars. Icarus 213, 451–472.
Ruesch, O., 14 colleagues, 2013. Seeing through the pyroxene: distribution of olivine-bearing material on Vesta using VIR/Dawn data. In: European Planetary Science Congress 2013. EPSC2013-891 (abstract).
Rugel, G., 9 colleagues, 2009. New measurement of the ^{60}Fe half-life. Phys. Rev. Lett. 103 (7), 072502.
Russell, C.T., 27 colleagues, 2012. Dawn at Vesta: testing the protoplanetary paradigm. Science 336, 6082, 684.
Russell, C.T., 23 colleagues, 2013. Dawn completes its mission at 4 Vesta. Meteorit. Planet. Sci., 1–14.
Ruzicka, A., Snyder, G.A., Taylor, L.A., 1997. Vesta as the howardite, eucrite and diogenite parent body: implications for the size of a core and for large-scale differentiation. Meteorit. Planet. Sci. 32, 825–840.
Samuel, H., 2012. A re-evaluation of metal diapir breakup and equilibration in terrestrial magma oceans. Earth Planet. Sci. Lett. 313–314, 105–114.
Schiller, M., Baker, J., Creech, J., Paton, C., Mullet, M.-A., Irving, A., Bizzarro, M., 2011. Rapid timescales for magma ocean crystallization on the howardite-eucrite-diogenite parent body. Astrophys. J. Lett. 740, L22, 6 pp.
Schubert, G., Turcotte, D.L., Olson, P., 2001. Mantle Convection in the Earth and Planets. Cambridge University Press, 940 pp.
Schwenn, M.B., Goetze, C., 1978. Creep of olivine during hot-pressing. Tectonophysics 48, 41–60.
Scott, T., Kohlstedt, D.L., 2006. The effect of large melt fraction on the deformation behavior of peridotite. Earth Planet. Sci. Lett. 246, 177–187.
Shearer, C.K., Fowler, G.W., Papike, J.J., 1997. Petrogenetic models for the origin of diogenites and their relationship to basaltic magmatism on the HED parent body. Meteorit. Planet. Sci. 32, 877–889.
Siggia, E.D., 1994. High Rayleigh number convection. Annu. Rev. Fluid Mech. 26, 137–168.
Sohl, F., Spohn, T., 1997. The interior structure of Mars: implications from SNC meteorites. J. Geophys. Res., Planets (1991–2012) 102, 1613–1635, E1.
Solomatov, V.S., 2007. Magma oceans and primordial mantle differentiation. In: Schubert, G. (Ed.), Treatise on Geophysics, vol. 9. Elsevier, pp. 91–120.
Sterenborg, M.G., Crowley, J.W., 2013. Thermal evolution of early solar system planetesimals and the possibility of sustained dynamos. Phys. Earth Planet. Inter. 214, 53–73.
Stevenson, D.J., 2003. Planetary magnetic fields. Earth Planet. Sci. Lett. 208, 1–11.
Stolper, E., 1975. Petrogenesis of euctire, howardite and diogenite meteorites. Nature 258, 220–222.
Stolper, E., 1977. Experimental petrology of eucrite meteorites. Geochim. Cosmochim. Acta 41, 587–611.
Takeda, H., 1997. Mineralogical records of early planetary processes on the howardite, eucrite, diogenite parent body with reference to Vesta. Meteorit. Planet. Sci. 32, 841–853.
Taylor, G.J., 1992. Core formation in asteroids. J. Geophys. Res., Planets (1991–2012) 97, 14717–14726, E9.
Telus, M., Huss, G.R., Ogliore, R.C., Nagashima, K., Tachibana, S., 2012. Recalculation of data for short-lived radionuclide systems using less-biased ratio estimation. Meteorit. Planet. Sci. 47, 2013–2030.
Tkalcec, B.J., Golabek, G.J., Brenker, F.E., 2013. Solid-state plastic deformation in the dynamic interior of a differentiated asteroid. Nat. Geosci. 6, 93–97.
Warren, P.H., 1997. Magnesium oxide–iron oxide mass balance constraints and a more detailed model for the relationship between eucrites and diogenites. Meteorit. Planet. Sci. 32, 945–963.
Wilson, L., Keil, K., 2012. Volcanic activity on differentiated asteroids: a review and analysis. Chem. Erde 72, 289–321.
Yomogida, K., Matsui, T., 1983. Physical properties of ordinary chondrites. J. Geophys. Res. 88, 9513–9533.
Zellner, B.J., et al., 1997. Hubble space telescope images of asteroid Vesta in 1994. Icarus 128 (1), 83.